Research Square

Preprints are preliminary reports that have not undergone peer review.
They should not be considered conclusive, used to inform clinical practice,
or referenced by the media as validated information.

Defect Engineering in Nd2Zr2O7 Pyrochlore via Synergistic Doping: DFT Predictions and Experimental Confirmation

A Ajayraj
National Institute of Technology Warangal
Anjana P Anantharaman
anjanapa@nitw.ac.in
National Institute of Technology Warangal

Research Article

Keywords: Pyrochlore, Dopant, Defect formation energy, DFT, Ionic conductivity

Posted Date: May 8th, 2026

DOI: https://doi.org/10.21203/rs.3.rs-9536375/v1

License: This work is licensed under a Creative Commons Attribution 4.0 International License.
Read Full License

Additional Declarations: No competing interests reported.

Defect Engineering in $Nd_2Zr_2O_7$ Pyrochlore via Synergistic Doping: DFT Predictions and Experimental Confirmation

A Ajayraj [a], Anjana P Anantharaman [a*]

[a] *Department of Chemical Engineering, National Institute of Technology Warangal, 506004, Telangana, India*

Corresponding Author Information:

*

Dr. Anjana P Anantharaman, Ph. D.

Assistant Professor, Chemical Engineering Department

National Institute of Technology Warangal,

Warangal-506004, India

E-mail: anjanapa@nitw.ac.in

Abstract

Functional energy materials are gaining importance as next-generation energy materials, including Solid Oxide Fuel Cell (SOFC) electrolytes that can achieve higher ionic conductivity at lower temperatures without sacrificing chemical and thermal stability. Pyrochlore ($A_2B_2O_7$) is a versatile functional material with a unique structure that can accommodate a variety of A- and B-site cations, enabling tuning of conductivity by adjusting oxygen vacancy concentration. The selection of dopants at the A- and B-sites is critical and extensive; this work uses DFT calculations to identify suitable cations and compositions for $Nd_2Zr_2O_7$ pyrochlore, thereby optimising defect formation energy (DFE). Based on the DFT calculations, $Nd_2Zr_{1.7}Mg_{0.3}O_7$ (NMgZO) and $Nd_2Zr_{1.7}Mo_{0.3}O_7$ (NMoZO) were found to be the optimised compositions of the B-site dopant, and $Nd_{1.94}Sm_{0.06}Zr_{1.7}Mo_{0.3}O_7$ (NSMoZO) was identified as the optimised co-dopant composition. Further, doped and co-doped pyrochlore samples of NMgZO, NMoZO, and NSMoZO were synthesised using the sol-gel method, characterised by XRD, SEM, EPR, and XPS, and tested for ionic conductivity. The conductivity study correlates with the defect formation energy trend: NSMoZO has the highest conductivity (0.0154 S/cm at 750 °C) and the lowest DFE (-5.7422 eV), followed by NMoZO (0.0152 S/cm at 750 °C) and NMgZO (0.0135 S/cm at 700 °C), and agrees with theoretical calculations. The enhanced conductivity stems from the creation of oxygen vacancies due to aliovalent doping, enhanced vacancy generation, and, by the B-site dopant, enhanced ion transport, as well as stability enhancement by the A-site dopant. The work contributes to setting DFE as a tool in designing the pyrochlore electrolyte, which would benefit from dopant selection.

Keywords: Pyrochlore, Dopant, Defect formation energy, DFT, Ionic conductivity

1. Introduction

Solid oxide fuel cells (SOFCs) are widely recognised as a clean and sustainable energy technology due to their high-energy conversion efficiency, 45-60 % while operating with natural gas and exceeds 70-90% in combined heat and power (CHP) system, fuel flexibility including, natural gas, biogas, and syngas beyond hydrogen fuel, and durability in extreme operating temperature (700-900^{o}C) with longer service life. The key challenge in SOFC application is the high operating temperature that results in slow start-up time, and long-term degradation, which necessitates lowering to intermediate-temperature SOFC (IT-SOFC) (600–800 °C) or low-temperature SOFC (LT-SOFC) (<650 °C), which offers distinct advantages over high-temperature SOFCs, including broader material selection, quick start-up, reduced thermal degradation, lower costs, and durability [1][2][3]. Nevertheless, the selection of materials, especially solid electrolyte materials capable of sustaining high oxygen-ion conductivity at intermediate temperatures, remains a significant challenge in advancing IT-SOFC performance [4][5]. Among the recently explored functional electrolytes, pyrochlore-type oxides ($A_2B_2O_7$) are emerging IT-SOFC electrolytes due to their thermal stability, structural adaptability, and efficient ion transport ability [5][6]. The inherent structural vacancy in pyrochlore facilitates ion mobility, making them suitable for electrochemical applications that require stable ionic conduction across various temperatures and oxygen partial pressures. A-site is generally occupied by larger cations with various oxidation states, such as Bi^{3+}, Cs^{+}, Pb^{2+}, among other rare earth metals and B-site cation is usually smaller and higher valence, such as Sn^{4+}, Zr^{4+}, Hf^{4+}, Te^{4+}, or Ti^{4+} [7] [8].

Broadly, zirconate- ($A_2Zr_2O_7$) and titanate-pyrochlores ($A_2Ti_2O_7$) are widely investigated electrolyte materials for IT-SOFC electrolyte applications due to the stability coupled with high ionic conductivity. $A_2Zr_2O_7$ pyrochlore (A = La, Ce, Nd, Gd) synthesized

via the sol-gel route was investigated in previous studies to assess the structural stability and ionic transport properties. $Nd_2Zr_2O_7$ (NZO) exhibited the highest ionic conductivity of 1.27×10^{-2} S/cm at 700 °C, surpassing $La_2Zr_2O_7$, $Ce_2Zr_2O_7$, and $Gd_2Zr_2O_7$ [9]. To further improve conductivity, the activation energy for ion migration should be reduced, along with an increase in mobile vacancy concentrations, which depend on the crystal structure. The preferential conduction pathway in a pyrochlore follows the tetrahedron plane around 48f cation sites, which can be tuned by modifying the crystal structure. Oxygen ion conduction in pyrochlore is predominantly governed by the formation and migration of oxygen vacancies, a process described by the defect reaction, represented by the Kroger-Vink **Equation 1** [10]:

$$V_O^{\cdot\cdot} + \frac{1}{2}O_2 \rightarrow O_O^{\times} + 2h^{\bullet} \qquad \textbf{[1]}$$

During the interaction of atmospheric oxygen with lattice oxygen vacancies $V_O^{\cdot\cdot}$, in pyrochlore results in forming oxygen lattice sites $O_O^{\times}$ along with holes $h^{\bullet}$, which is crucial in influencing the ionic conductivity [10]. To improve the vacancy formation, suitable dopant addition to pyrochlore lattice is advantageous as it modifies the lattice energies and introduces oxygen vacancies. Substitution of lower-valent cation (Ca^{2+}, Sr^{2+} or Ba^{2+}) in A^{3+} site would offer better ionic conductivity due to charge compensation effect, B-site doping would distort the phase or unit cell and improve oxygen mobility and co-doping on both sites also would offer improved performance due to synergistic defect formation [11] [12].

Previous reports have demonstrated the efficacy of doping in enhancing oxygen ion conduction. Liu et al. [13] reported that Mg-doping up to 15 mol% in $GdSmZr_2O_6$ significantly improved sintering and ionic conductivity, increasing from 1.01×10^{-4} S/cm to 1.29×10^{-3} S/cm with the doping at 1173 K [13]. Moreno et al. [14] observed that increasing Zr content in $Gd_2(Zr_xTi_{1-x})_2O_7$ enhanced the concentration of mobile oxide ions, although this was accompanied by higher activation energies for long-range ion transport [14]. Mandal et al. [15]

showed that the partial substitution of Gd by Nd in $Gd_2Zr_2O_7$ resulted in nearly an order of magnitude increase in ionic conductivity [15]. Xia et al. [16] found that selective doping with smaller cations at Zr sites or larger cations at Gd sites enhanced oxide-ion ordering and improved ionic conductivity, while excessive disorder at these sites further promoted oxygen-ion mobility [16]. Co-doping A and B sites will provide more pathways for the oxide ion and generate more vacancies. Radhakrishnan et al. [17] investigated co-doped pyrochlore solid solutions of the form $(Ca_xGd_{1-x})_2(Zr_{1-x}M_x)_2O_7$ (M = Nb, Ta; x = 0.1–0.5), synthesized via solid-state methods.

The computational works, notably those by Liu et al. [18], demonstrated that optimized cation distributions and lattice engineering approaches could dramatically reduce ion migration barriers and improve room-temperature ionic conductivities in solid electrolytes. For example, the transformation of $Na_3Zr_2Si_2PO_{12}$ (NZSP) to $Li_3Zr_2Si_2PO_{12}$ (LZSP) via DFT-guided cation exchange reduced the migration barrier from 0.53 eV to 0.29 eV, resulting in a substantial conductivity enhancement to 3.59×10^{-1} S/cm. Their work highlighted the predictive capability of DFT in rationally designing solid electrolytes with improved ionic transport properties [18].

The literature review confirms that, dopant selection is critical in deciding the ionic conductivity behaviour of pyrochlore, the extended fluorite structure of pyrochlore has a unique ability to fit a wide range of cations with the ability to deliver improved electronic properties. Extensive experimental studies have examined the effects of individual A-site or B-site doping in pyrochlore oxides using a range of cationic species, with a primary focus on their structural and electrical modifications. However, the effects of co-doping remain less comprehensively explored, particularly in the context of cation disorder, defect chemistry, and ionic conductivity. Despite the promising potential of doping, experimentally evaluating all possible dopant and co-dopant combinations is both costly and time-consuming. First principle

calculations was extensively studied to estimate the oxygen vacancy defect formation in materials for the prediction of ion conductivity and thus the design of the materials [19], however dopant and co-dopant selection based on defect formation energy is not reported in the literature. This computational screening, supported by Ab Initio Molecular Dynamics (AIMD) simulations, will provide detailed insights into defect structures, ion migration mechanisms, and activation energy profiles, enabling targeted experimental validation while significantly reducing material and resource use.

2. Materials and methods

2.1. Dopant Selection through DFT Analysis

Density functional theory (DFT) calculations were performed using Burai version 1.3.2 to identify the most effective dopant for $Nd_2Zr_2O_7$ (NZO). Nine B-site dopants were assessed at concentrations of 10%, 15%, and 20% to determine the optimal dopant type and loading. Following the selection of the B-site dopant, A-site doping was conducted with nine different dopants at concentrations of 3.125%, 6.25%, and 12.5%. Dopants that satisfy the radius ratio condition (R_A/R_B = 1.46-1.78) for a stable pyrochlore structure was only selected in the study. The dopant concentration on B-site was chosen based on the generally reported concentration range and A-site dopant was chosen such that the crystal symmetry is maintained along with the lower concentration range. **Figure 1** illustrates NSMoZO containing 3.125% Sm doped on the A-site and 15 % Mo doped on the B-site. **Table 1** presents the electronic valence configurations of the elements utilised in the calculation. The energy associated with defect generation serves as a vital factor that directly indicates the stability of the structure and its influence on the concentration. The calculations employed the projector-augmented wave approach (PAW) and the generalized gradient approximation Perdew Burke and Ernzerhof

(GGA-PBE) exchange-correlation functional along with ultrasoft pseudopotentials. For the computations, the plane wave energy cut-off was set at 225 eV, the energy convergence criterion was assumed to be 10^{-5} eV along with a 1 x 1 x 1 mesh, and the Monkhorst-Pack approach was used. All the calculations were performed in Burai 1.3, a GUI system of Quantum ESPRESSO, and crystal structures were generated using Vesta Software. The supercells consist of 96 atoms, considering structural relaxations at zero pressure. All calculations included spin polarisation. The energy cut-offs for the plane waves in NMgZO, NMoZO, and NSMoZO are 58.12, 49, and 49 Ry, respectively. The grid of points, the threshold for convergence, and other relevant parameters for the calculations were presented in **Table S1**. The potentials of cations and anions are interconnected and linked to the total energy of the pyrochlore sample [20]. The addition of dopants to the system is presumed not to affect the chemical potential of oxygen. Moreover, the thermal, vibrational, and entropic contributions were neglected, as they are considered less significant compared to the standard DFT error. It is crucial to note that in real materials, these properties are affected by both temperature and the partial pressure of oxygen, which can have a direct impact on these values. The energy associated with the formation of oxygen vacancies (O_{48f}) was determined using **Equation 2**.

$$\mathbf{E_v = E_d + \frac{1}{2}E_{O_2} - E_p} \qquad \mathbf{[2]}$$

In this context, E_d, E_{O2}, and E_p denote the energy associated with a single oxygen vacancy defect within the system, the free energy of the oxygen molecule, the free energy of an oxygen molecule refers to the energy of an oxygen atom positioned within a large lattice, achieved through relaxation equilibrium (-1.6 eV), and the energy of the ideal system, respectively [21]. Reduced E_v values suggest enhanced mobility of oxygen ions and improved stability in doping processes.

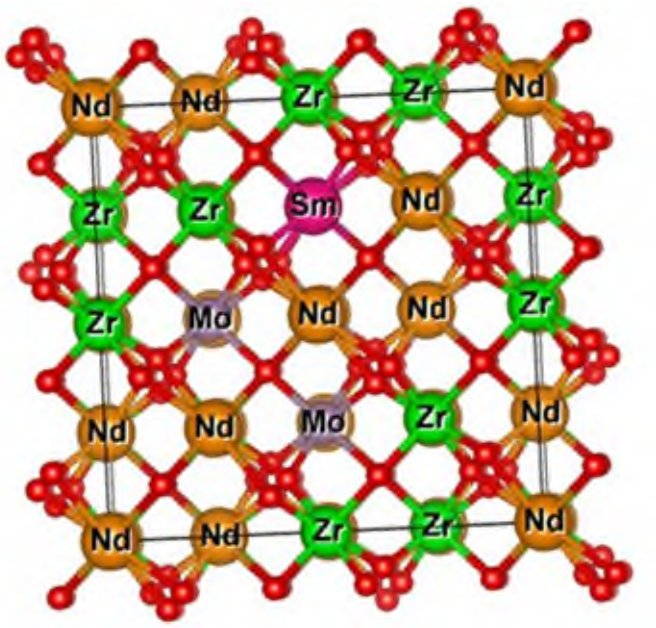


Figure 1: Illustration of Crystal structure of NSMoZO.

Table 1: Valance configurations of the elements

Element	**Electronic configuration**
Nd	$6s^2\ 6p^0\ 5d^0\ 4f^4$
Sm	$6s^2\ 6p^0\ 5d^0\ 4f^6$
Zr	$5s^2\ 5p^0\ \ 4d^2\ 4f^0$
Mg	$3s^2\ 3p^0\ 3d^0\ 4f^0$
Mo	$5s^2\ 5p^0\ 4d^4\ 4f^0$
O	$2s^2\ 2p^4\ 3d^0\ 4f^0$

2.2. Material synthesis:

NZO samples incorporating 15% Mg or Mo at the B-site (Zr) were synthesised using the sol-gel technique. For the preparation of $Nd_2Zr_{1.7}Mg_{0.3}O_7$ (NMgZO), Magnesium nitrate hexahydrate ($Mg(NO_3)_2.6H_2O$, SRL chemicals), Neodymium nitrate hexahydrate ($Nd(NO_3)_2.6H_2O$, SRL chemicals), Zirconium (IV) oxynitrate hydrate ($Zr(NO_3)_2.6H_2O$, Sigma Aldrich), metal precursors were used. Instead of Magnesium salt, Molybdenum(V) chloride ($MoCl_5$, SRL chemicals) was used along with other metal precursors for $Nd_2Zr_{1.7}Mo_{0.3}O_7$ (NMoZO) synthesis and co-doped $Nd_{1.94}Sm_{0.06}Zr_{1.7}Mo_{0.30}O_7$ (NSMoZO) samples were synthesized using all the metal precursors along with Samarium nitrate hexahydrate ($Sm(NO_3)_3.6H_2O$, SRL chemicals). Metal nitrates were combined with ethanol (RCP chemicals) and citric acid (Finar chemicals) at a 5:2 ratio for the citric acid: metal nitrate. The solution underwent heating at 80 °C to facilitate gel formation, followed by drying at 120 °C. Calcination involved heating the dried gel at 350 °C for a duration of 24 h, followed by an elevation to 800 °C for 2 h to facilitate the formation of the pyrochlore phase. The powder underwent a process of pelletising and sintering, where it was pressed into pellets and subsequently subjected to a temperature of 1150 °C for a duration of 5 h [9]. This procedure aimed to enhance the structural integrity and density of the material.

2.3. Material characterization

Powder X-ray diffraction (PXRD) patterns of the sintered samples were recorded using an XPERT-PRO diffractometer equipped with Cu Kα radiation (λ = 1.54 Å), over a 2θ range of 20° to 80°, in powder form for a sampling time of 30 minutes for each sample, to analyze the crystallographic structure of the pyrochlore phase. Morphological analysis of both calcined and sintered powders was performed using a JEOL JSM-IT800 Field-Emission Scanning Electron Microscope (FE-SEM) operated at 8 kV, powder samples were subjected to Au sputter coating with a thickness of 7 nm. Energy Dispersive X-ray Spectroscopy (EDS) was conducted

in vacuum mode on the sintered powders at a landing voltage of 6 kV to analyze elemental distribution. Electron Paramagnetic Resonance (EPR) spectra were recorded at room temperature on a JEOL RESONANCE Inc. JES-FA100 spectrometer operating in the X-band (~9.4 GHz). Finely ground doped samples were sealed in quartz tubes for evaluating g-values, line widths, and defect signatures. X-ray Photoelectron Spectroscopy (XPS) was performed on the sintered ceramics using a Kratos AXIS Supra system with a monochromatic Al Kα source with – 1486.6 eV to analyze surface elemental states. All samples XPS spectra, were calibrated to the C 1 s peak at 284.8 eV, O 1 s spectra were deconvoluted using CasaXPS software with Gaussian peak fitting and plotted using OriginPro software. All the equations used for the calculations can be found in the Supplementary File.

2.4. Analysis of Conductivity:

The ionic conductivity of the samples was assessed utilising a two-probe configuration linked to a Keithley 2450 source meter. A direct current (DC) was introduced via one probe, while the resultant voltage was recorded through the other probe. The measurements were performed across a temperature spectrum of 550–900 °C, employing a heating rate of 10 °C per minute, with data collected at 50 °C intervals. The Keithley 2450 source meter was used for the resistance measurements. The ionic conductivity was calucalted using the observed resistance value at varying temperature using **Equation 3** [22] and the activation energies was evaluated using the following Arrhenius **Equation 4** [23]

$$\boldsymbol{\sigma = \frac{L}{Re * A}} \qquad \textbf{[3]}$$

$$\boldsymbol{\sigma = \frac{k}{T} \exp\left(\frac{-E}{RT}\right)} \qquad \textbf{[4]}$$

Where σ is the ionic conductivity (S/cm), Re is the measured resistance (Ω), L is the thickness of the pellet (cm), and A is the cross-sectional area of the pellet (cm^2). σ represents

the ionic conductivity measured in S/cm, *k* is the pre-exponential factor with units of S·K/cm, *T* is the absolute temperature in Kelvin (K), *E* is the activation energy for conduction expressed in J/mol, and *R* is the universal gas constant, valued at 8.314 J/mol·K.

3. Results and discussion

3.1. Dopant selection:

The energy for oxygen vacancy formation was estimated by first substituting a dopant at the B-site, followed by A-site dopant addition, which leads to co-dopant formation. The dopant selection based on Defect Formation Energy (DFE) is discussed in detail for various dopants as dopant and co-dopant.

3.1.1. B-site dopant selection:

The Defect Formation Energy (DFE) was adopted as a guide for dopant selection in the host NZO pyrochlore matrix, further the DFE was correlated with the ionic conductivity values and analysed for tuning the dopant type. The dopant chosen were based on the previously reported cations along with the analysis of oxidation state and ionic radius as per radius ratio conditions (r_A/r_B). The substation of cation with different oxidation state would lead to charge compensation mechanism that result in adjusting the bond angle and length to ensure stability of the system, this consequently results in oxygen vacancy and dopant binding that has an inverse relation with ionic radius and vacancy migration [24]. Dopant like Li^+ (ionic radius: 0.76 Å), will introduce substantial charge imbalance compared to Zr^{4+} promoting oxygen vacancy formation; at higher concentration the lattice destabilises with poses a potential drawback [25]. Divalent dopants (Mg^{2+} (0.72 Å), Ca^{2+} (1.00 Å), and Sr^{2+} (1.18 Å)) would also promote charge imbalance and thus reported well in the literature. Large ionic radius cation

like, Ca^{2+} and Sr^{2+} would widen the oxygen migration channel through lattice distortion, in contrary smaller ionic size Mg^{2+} generates an oxygen vacancy while preserving lattice stability [26, 27][28]. Trivalent cations such as Yb^{3+} (0.868 Å) [29] and tetravalent dopants, including Ti^{4+} (0.605 Å) and Ce^{4+} (0.97 Å), were selected for their ability to induce local lattice distortions that facilitate ion mobility. Even higher valent dopants like Mo^{6+} (0.59 Å) and V^{5+} (0.54 Å) were included since the oxygen vacancy may be predominant due to significant charge difference and small ionic size. With this background, a total of 9 dopants were selected, namely, V, Ti, Mo, Mg, Li, Yb, Ce, Ca and Sr, respectively. Generally, B-site dopant loading is reported in the range of 10-20 mol%. Each dopant of 10, 15, and 20 mol% was loaded to the NZO lattice, and the corresponding DFE was estimated.

The heatmap representing the variation in DFE with the dopant nature and dopant concentration is plotted for the B-site doping in **Figure 2,** and the values are tabulated in **Table S2**. The dopant order considered in the vertical axis of the heatmap is with the increase in ionic radius, implying smaller ionic radius V is on the bottom, and the larger ionic radius Sr is on the top of the figure. For reference, the undoped NZO sample exhibited a baseline DFE of –5.45 eV [9]. The formation energies of all oxygen vacancies were consistently negative, suggesting that the development of defects is energetically favourable with respect to the hole-compensation mechanism. Nakamura et al. [30] demonstrated a vacancy formation energy of approximately −6 eV for the $Gd_2Ti_2O_7$ sample's O_{48f} site at the zero Fermi energy level, aligning with our computed DFE values [30]. Ti, Mo, Mg, Yb, and Ce have shown DFE lower than that of the undoped NZO sample, essentially these dopants has an ionic radius near to Zr^{4+}, and the dopants are at least divalent. In this case, an intermediate concentration of dopant (15 %) indicates relatively lower DFE compared to higher (20 %) and lower (10 %) dopant concentrations, implying ease of oxygen vacancy formation. This observation is in line with

the literature, as the widely reported dopants in the literature are: Mg [31, 32], Ce [16][33][34], Ti [34, 35] [35] [36], Mo [37].

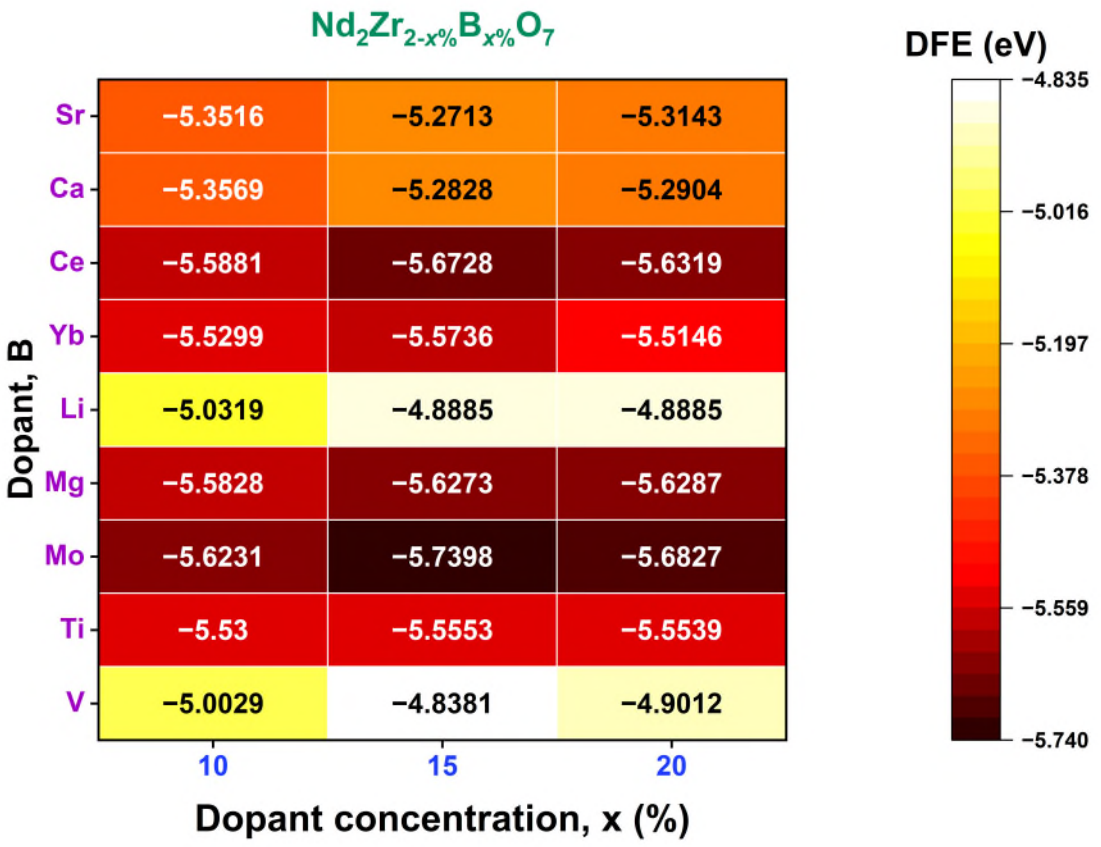


Figure 2: Heatmap of the DFEs of the B-site doped NZO samples.

While other dopants like, Li, Ca and Sr, having larger ionic radius difference with Zr^{4+} and lower oxidation state shows higher DFE compared to undoped samples, especially with 15 mol% doping. Even, smaller ionic radius of V also resulted in a higher DFE value. V, Ca and Li [38][39] are also reported in the literature but DFE shows a higher value. This trend in values confirms that the dopant selection is not only dependent on ionic radius or oxidation state, rather a combination of both along with other parameters like electronic structure, redox potential and electronic structure. Among all the dopants, 15 % Mo shows the lowest DFE of

-5.739 eV. This superior performance could be attributed to a small ionic radius (0.59 Å) and the highest oxidation state (6+) of Mo. Moreover, Mo substitution in pyrochlore has been reported to improve conductivity under intermediate loading conditions in $Gd_2Ti_2O_7$ due to a lower band gap, which further reduces the Fermi energy for oxygen transport [40] Similarly, Mg loading of 15% (–5.6273 eV) and 20% (–5.6287 eV) has shown competitive DFE values primarily due to improvement in anion vacancy formation with the divalent cation substitution [41] Following Mo and Mg, Ce-doping yields relatively low DFE at 15 % (-5.673 eV), however, the DFE rises further at 20 %, indicating the loss of vacancy-stabilization. Moreover, the multiple oxidation states of Ce would yield mixed ionic-electronic conductivity that is not favorable for an electrolyte. Across all the dopants selected, it is evident that 15% doping is optimal, which essentially balances the oxygen vacancy generation and lattice stability. Among all candidates, Mo^{6+} and Mg^{2+} emerged as the most promising B-site dopants for NZO, with Mo^{6+} offering superior oxygen vacancy formation capabilities, while Mg^{2+} presents a thermodynamically stable and structurally reliable alternative. Further, the co-doping at A-site with B-site substituted with Mo and Mg on NZO lattice was studied by optimizing the DFE. From now on, the notation NMoZO will represent Mo doped NZO and NMgZO will represent Mg doped NZO, respectively.

3.1.2. Selection of co-dopant:

Similar to the B-site dopant selection, a range of A-site dopants were selected based the radius ratio condition and literature reported dopants. Nine rare-earth trivalent cations—Hf^{3+} (0.85 Å), Er^{3+} (0.89 Å), Ho^{3+} (0.901 Å), Dy^{3+} (0.912 Å), Gd^{3+} (0.938 Å), Eu^{3+} (0.947 Å), Sm^{3+} (0.958 Å), Pm^{3+} (0.965 Å), and Pr^{3+} (0.99 Å)—were selected based on their ionic radii and ability to induce controlled lattice distortions without disrupting charge balance. Co-doping

concentrations of 3.125%, 6.25%, and 12.5% were examined through defect formation energy (DFE) calculations for NMoZO and NMgZO such that the structural symmetry is being maintained. The literature reports mostly 2-10% of A-site doping, thus the atomic substation on an NZO pyrochlore by maintaining the structural symmetry has resulted in the co-dopant concentration selection. The DFE value was estimated for the co-doped NZO substituted with Mg and Mo in the B-site, and the respective heatmaps are shown in **Figure 3 (a)**, and **Figure 3 (b)**. Similar to B-doped sample heatmap, the ionic radius of co-dopants in heatmap increases along the y-axis. DFE of the co-doped sample has only a slight increase in value compared to the doped samples. The electronic properties is reported to be improved by the B-site doping and the ionic conductivity is expected to be affected by A-site doping [42]. Thus, the improvement in DFE with co-doping could be related to enhancement in oxygen vacancy formation.

Co-doping on NMoZO shows lower DFE compared to NMgZO due to the high oxidation state and strong oxygen sublattice interaction of the Mo dopant. Among all the samples analysed, the lower co-dopant concentration has relatively lower DFE compared to higher concentrations since the lattice distortion is minimum in the former case. For NMoZO, with the increase in ionic radius, the DFE values are lower, with Pm and Sm showing the lowest DFE. This could be related to the observation that the A-site dopant with a lower ionic radius mismatch would achieve higher ionic conductivity due to lower solution energy [43]. 3.125 % substitution of Sm^{3+} on the A-site has shown consistently lower DFE (–5.6797 eV for NMgZO and –5.7414 eV for NMoZO), indicating favorable oxygen vacancy formation and stable lattice structures. The similar ionic radius of Sm^{3+} and Nd^{3+}, minimizes the lattice strain while stabilizing the defects. minimizing lattice strain while effectively stabilizing defects. Smaller dopants like Er^{3+} and Ho^{3+}induced excessive contraction, while larger dopants such as $Eu^{3+}$and Pr^{3+} showed higher DFEs and reduced stability.

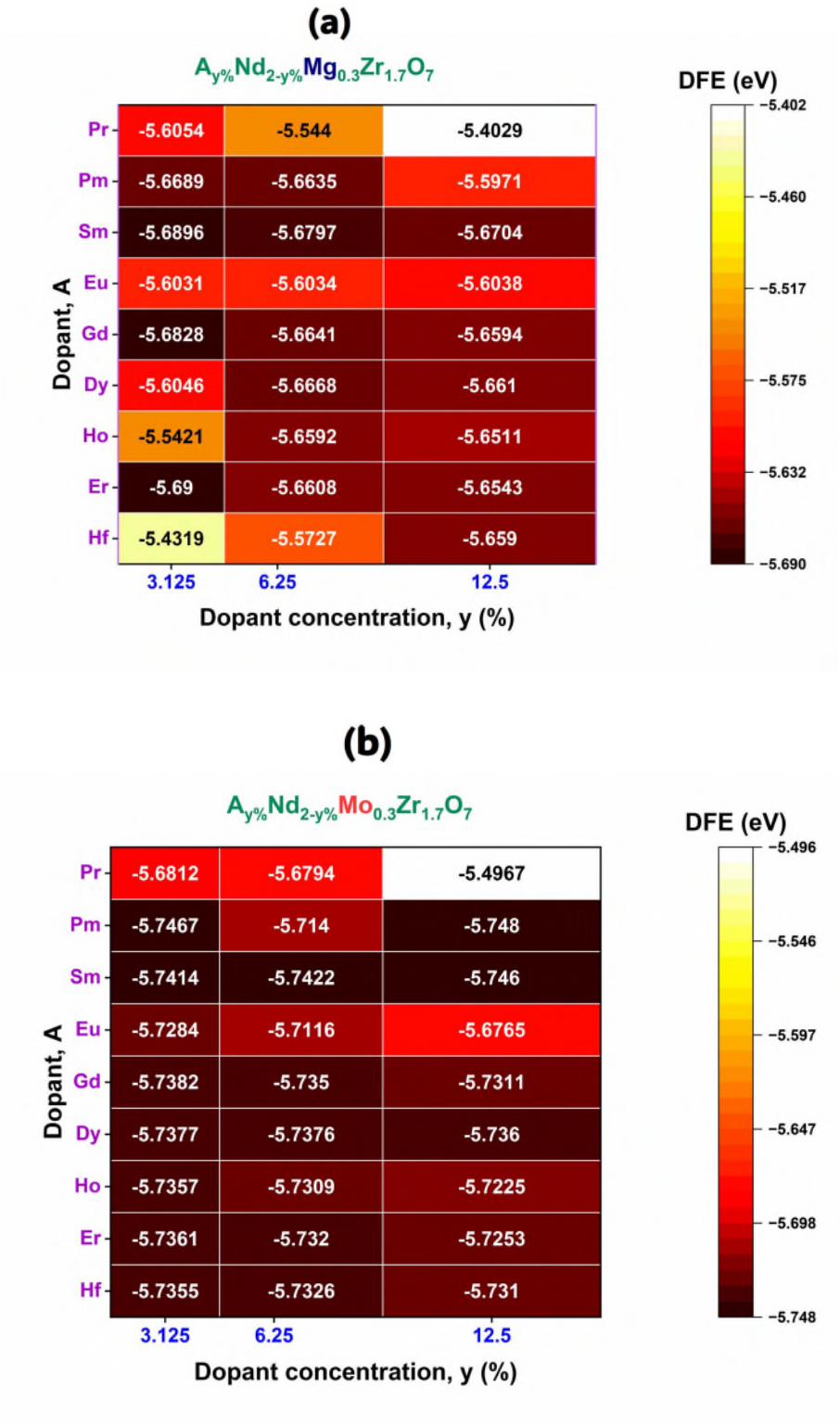


Figure 3: **Heat map of the DFEs of A-site dopant for a) NMgZO, b) NMoZO.**

Overall, doping Mo^{6+} (15%) at the B-site and co-doping Sm^{3+} (3.125%) at the A-site has shown the optimized oxygen vacancy formation based on DFE calculation and would

probably enhance ionic conductivity by maintaining structural integrity. According to theoretical calculations it is very well evident that B-site dopant influences the ion migration and thus the vacancy formation, however A-site dopant has an insignificant role in the vacancy formation. O_{48f} ion in a pyrochlore is surrounded by two A cations and two B cations. However, the B-O bond strength influences the 48f-48f oxygen hopping mechanism and thus the ionic conductivity of the pyrochlore oxide [17]. The DFE calculations do not consider the ionic conductivity directly; rather the vacancy formation energy was used as a tool to investigate the effect of dopant concentration and dopant cation. Even the incremental changes in DFE are evident for A-site doping compared to B-site dopants, which necessitates the ionic conductivity study to validate the theoretical results and confirm the role of dopant on A and B-sites.

3.2. Phase confirmation: X-Ray Diffraction

The optimized A-site and B-site dopants, as confirmed from DFT calculations: $Nd_2Zr_{1.7}Mg_{0.3}O_7$ (NMgZO), $Nd_2Zr_{1.7}Mo_{0.3}O_7$ (NMoZO), and $Nd_{1.94}Sm_{0.06}Zr_{1.7}Mo_{0.3}O_7$ (NSMoZO), were developed using the sol-gel method as per the stoichiometric composition. The developed samples were characterized using different tools to confirm the phase, structure and validate the ionic conductivity performance. The powder X-ray diffraction (PXRD) patterns (**Figure 4**) NMgZO, NMoZO, and NSMoZO confirm the formation of a cubic pyrochlore phase (space group: $Fd\bar{3}m$) in all samples [44]. Prominent fluorite-type reflections ((222), (400), (622)) along with superlattice peaks ((111), (311), (331)) validate the pyrochlore structure consistent with the reference pattern (PDF#00–017–0458) [45][46]. All doped sample shows consistent superstructure peaks confirming the disorder in pyrochlore with doping. The detailed XRD analysis was performed and the results are tabulated in **Table 2**.

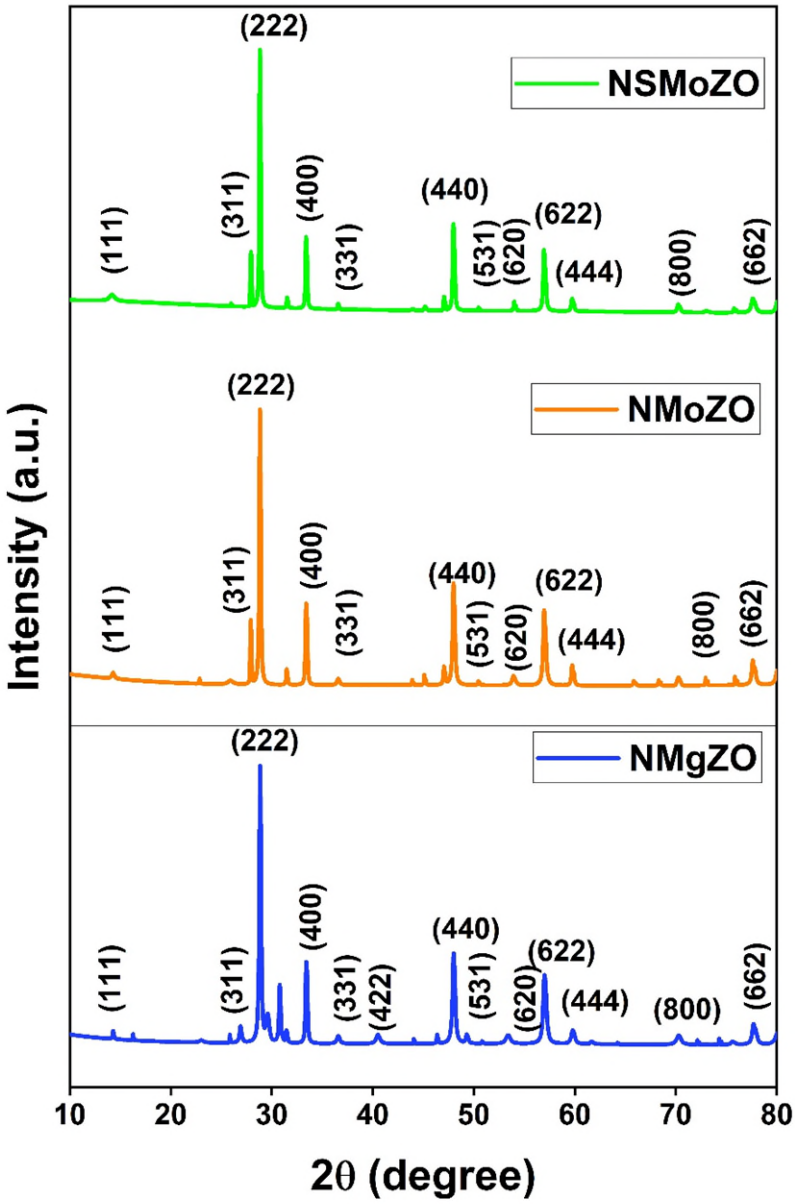


Figure 4: **PXRD spectrum of the doped samples**

The marginal increase in lattice parameter along with slight shift in (222) peak towards the lower angle for co-doped NSMoZO and NMoZO compared to NMgZO confirms the lattice contraction with the substitution of smaller dopant at the Zr^{4+} site. The dislocation density and

lattice strain evaluated further support these structural changes. NSMoZO shows the lowest dislocation density and lattice strain and highest relative density compared to NMoZO and NMgZO, indicating significant structure distortion with co-doping as they reduce defect clustering and enhance lattice coherence [47]. The XRD analysis confirms that co-doping improves the dopant accommodation in the complex pyrochlore structure without phase and structural distortion, confirming that the A-site dopant offers phase stability [48]. To confirm this, the degree of structural ordering was determined by the intensity ratio $I_{(111)}/I_{(222)}$. The ordering degree systematically decreases upon B-site doping, indicating a loss of cation ordering and the introduction of lattice defects [49]. NMgZO shows a higher ordering (0.018) compared to NMoZO (0.014), suggesting that Mo^{6+} substitution at the Zr^{4+} site generates significant disorder and oxygen vacancies due to its higher charge and smaller ionic radius, which supports the selection of Mo as B-site dopant in further for co-doping. In the co-doped NSMoZO sample ($I_{(111)}/I_{(222)}$= 0.016), the partial substitution of Sm^{3+} at the A-site (Nd^{3+} site) effectively compensates for the structural disorder induced by Mo^{6+}, thereby stabilizing the lattice [50]

Table 2: Lattice parameter, dislocation density, lattice strain and density calculation for doped and co-doped NZO pyrochlore

Material	**Lattice Constant(Å)**	**Dislocation Density (line/m^2) ×10^{-12}**	**Lattice strain**	**Ordering degree (111/222)**	**Theoretical density (kg/m^3)**	**Relative density (%)**
NMgZO	10.710	3.073	0.0036	0.018	6.086	91.8
NMoZO	10.715	3.604	0.00307	0.014	6.319	95.2

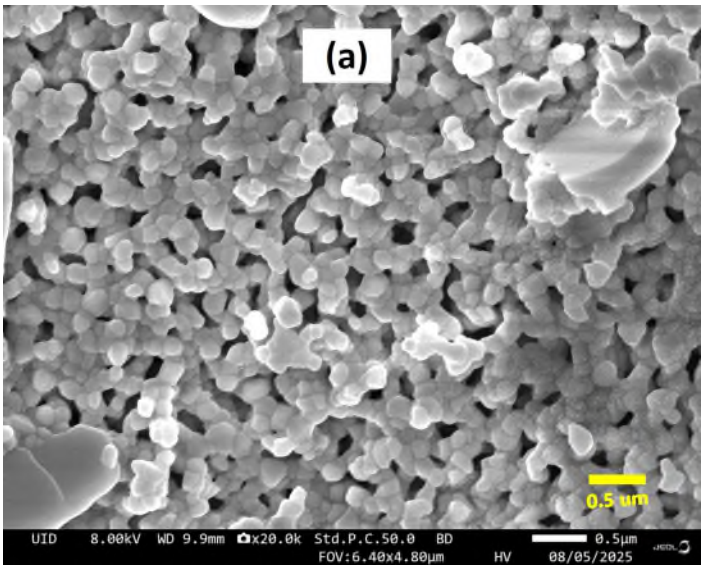
NSMoZO	10.716	0.379	0.00283	0.016	6.310	97.1

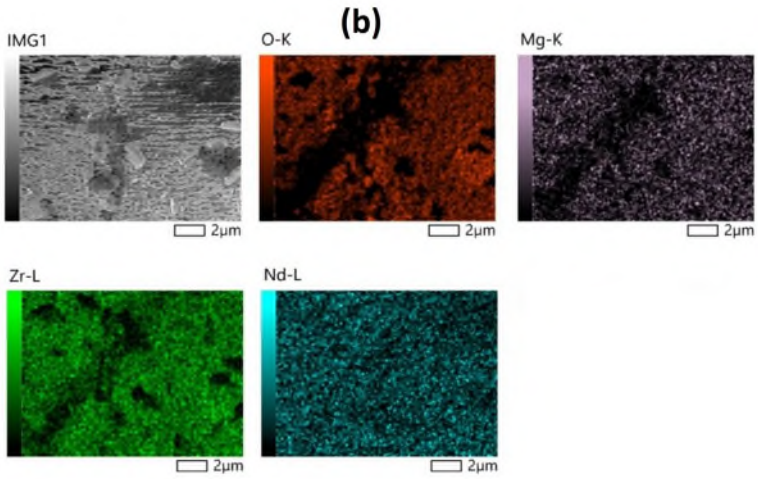
XRD analysis confirmed the phase purity and crystallographic structure of the samples. It is very well evident that doping and co-doping could result in lattice expansion and cation disordering, that promotes oxygen vacancy formation by lowering the ion migration barrier, thereby improving the ionic conductivity. Here, NSMoZO generates defect by structural stability which would probably improve the ionic conductivity. To correlate the relative density upon structure, the detail surface morphology analysis was performed using FESEM analysis.

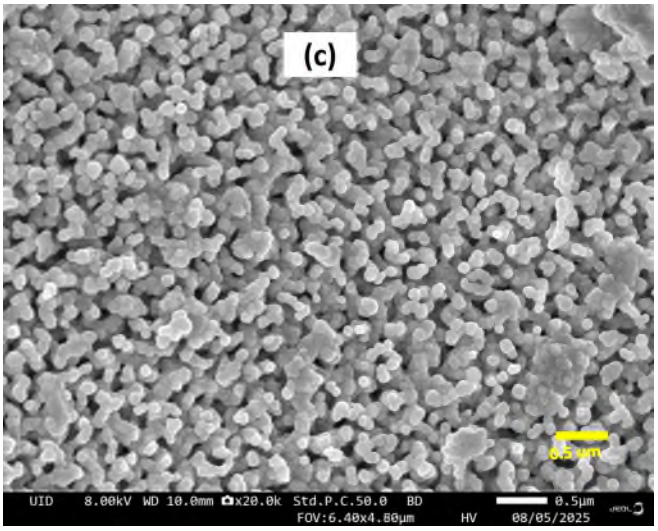
3.3. Morphological studies

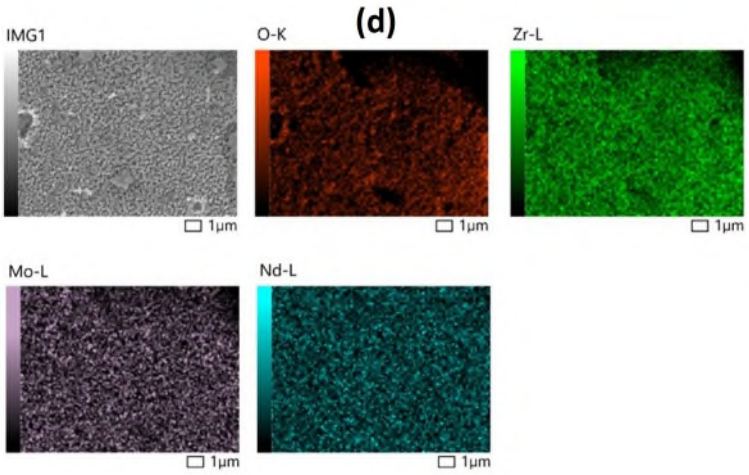
Figure 5 shows the Field Emission Scanning Electron Microscopy (FESEM) patterns of the doped and co-doped samples. The NMoZO and NMgZO show agglomerated spherical particles forming continuous pathway across the grains with NMoZO showing the smaller particles compared to NMgZO. Both the case, the interstitial pores are visible between the particles confirms more grain boundaries. Co-doped NSMoZO shows an aggregated plate-like structure with limited grain boundaries and porosity that is consistent with the improved relative density of the sample, suggesting enhanced sinterability through co-doping. FESEM-EDS mapping (**Figure 5** and **Table 3**) confirmed uniform distribution of Nd, Zr, O, and dopants across all samples. However, NMgZO exhibited a significant deviation in Mg content (0.05 wt%) from the theoretical value (1.294 wt%), indicating limited Mg solubility and potential challenges in achieving the desired defect chemistry. In contrast, NMoZO and NSMoZO shows consistent composition for measured and theoretical dopant levels, suggesting homogenous metal distribution as per stoichiometry. In line with XRD observation, the SEM images

confirms that co-doped sample is better than doped samples. To further probe dopant behavior, oxygen vacancy formation, and valence state fluctuations, advanced spectroscopic techniques such as XPS, and Electron Paramagnetic Resonance (EPR) are crucial for elucidating the electronic environments that govern the functional performance of these materials.






(c)
0.5 μm
UID 8.00kV WD 10.0mm x20.0k Std.P.C.50.0 BD
FOV:6.40x4.80μm
0.5μm
HV 08/05/2025


(d)
IMG1
O-K
Zr-L
Mo-L
Nd-L
1μm
1μm
1μm
1μm
1μm

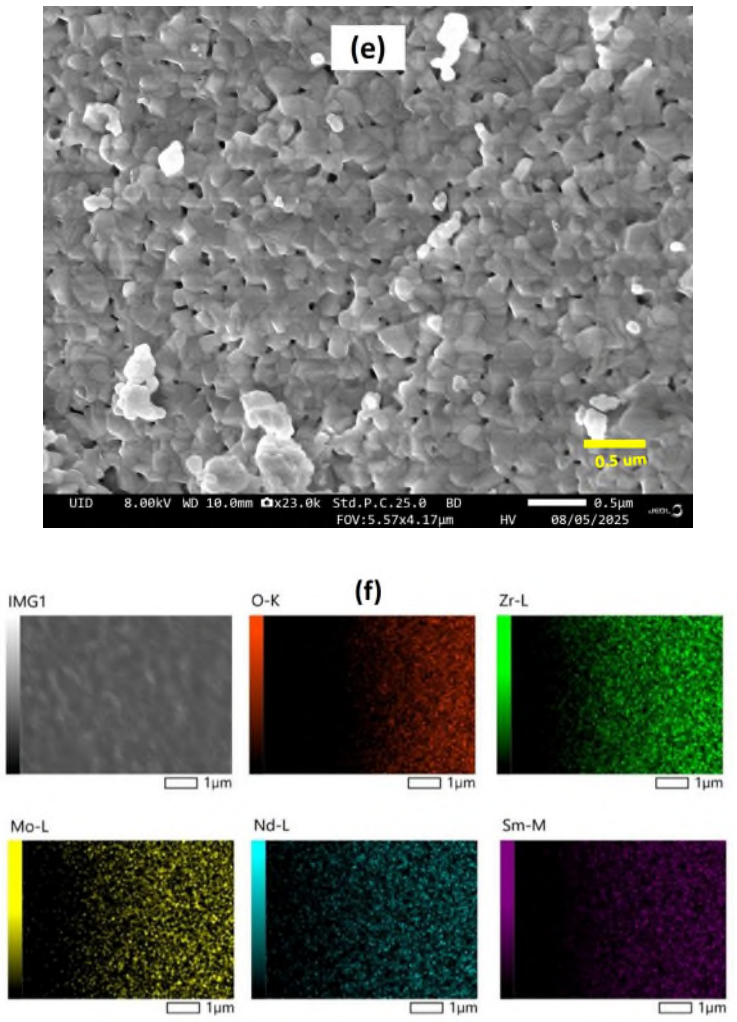


Figure 5: (a) FE-SEM images of NMgZO and (b) NMgZO mapping, (c) FE-SEM image of NMoZO and (d) NMoZO mapping (e) NSMoZO SEM image and (f) NSMoZO mapping.

Table 3: Comparative data of mass of elements from EDS and theoretical data

Sample	**NMgZO**		**NMoZO**		**NSMoZO**	
Element	**Theoretical mas%**	**EDS mas%**	**Theoretical mas%**	**EDS mas%**	**Theoretical mas%**	**EDS mas%**

Nd	51.253	57.85	49.368	54.07	47.857	51.568
Zr	27.563	23.87	26.537	23.05	26.521	23.458
O	19.89	18.243	19.169	18.55	19.154	20.924
Mg	1.294	0.05	-	-	-	-
Mo	-	-	4.926	4.33	4.922	2.55
Sm	-	-	-	-	1.543	1.5
g-factor	2.2081		2.189		2.2092	

3.4. Electron Paramagnetic Resonance (EPR):

The oxygen vacancy concentration and distribution is estimated using Electron Paramagnetic Resonance (EPR) spectroscopy for all the samples and represented in **Figure 6** [51]. The distinct paramagnetic resonance signal evident across all the samples with similar trend confirms the presence of unpaired electrons trapped in oxygen vacancies that is essential in facilitating the ion migration. The g-factor values of the samples are presented in **Table 3**, and it span from 2.189 for NMoZO to 2.2092 for NSMoZO. The intrinsic oxygen vacancy along with extrinsic vacancy created by dopants The g-factor is highest for NSMoZO (2.209) followed by NMgZO (2.208) and NMoZO (2.189), indicates the improved oxygen vacancies created with co-doping relative to dopant addition. The synergistic doping of Sm and Mo in A and B-site, respectively results in charge compensation, lattice destabilization and thereby improved vacancy formation. On the other hand, lower g-factor for NMoZO could be due to limited vacancy formation or localized vacancy distribution. The EPR results reaffirm the

observations of DFE calculations that confirms the selection of the dopant through DFE calculation is accurate in predicting the ease of vacancy formation. To further quantify their concentration, XPS analysis—particularly the deconvolution of the O 1s spectra—was employed.

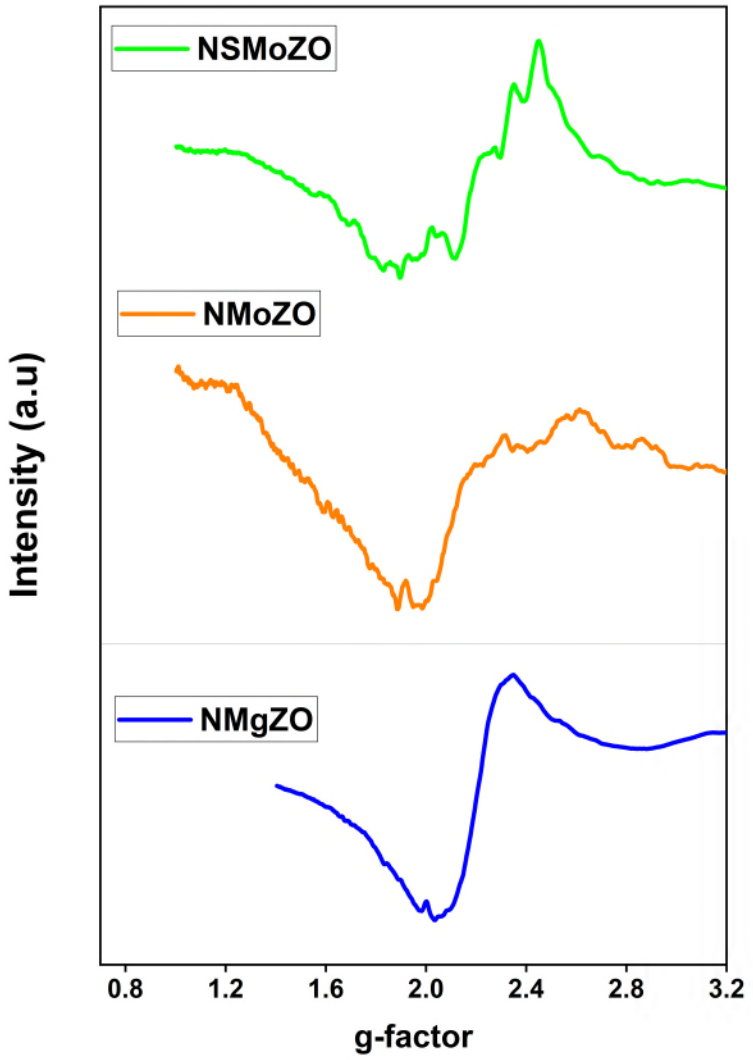


Figure 6: EPR spectrum showing g-factor of all the doped samples

3.5. X-ray photoelectron spectroscopy (XPS) Analysis

The O1s core level X-ray photoelectron spectroscopy (XPS) analysis of the doped and co-doped pyrochlore (NMgZO, NMoZO, and NSMoZO) (shown in **Figure 7**) were conducted to probe the local chemical environment of oxygen in the pyrochlore lattice and thus study the ion migration ability which correlates the ionic conductivity. Across all the samples, oxygen occupies two crystallographic sites: six out of every seven oxygen ions sit at the 48f positions with each bonded to two A-cations and two B-cations, while the remaining ion resides at the 8a site surrounded by four A-cations. Because the Nd–O interaction is more ionic (Nd/Sm) being less electronegative than Zr/Mg), oxygen at the 8a site carries a higher electron density and thus appears at lower binding energy in the O1s spectrum. Conversely, the 48f oxygen shows up at higher binding energy [52]. Deconvolution of the spectrum reveals Gaussian peaks at ~528 eV (8a site) and a higher binding energy peak at ~531 eV. To analyse the each oxygen site concentration the area ratio of $O_{8a}/(O_{8a} + O_{48f})$ was estimated for all the samples. The spectral separation suggests a relatively ordered structure with well-defined oxygen environments. NMgZO shows the two distinct peak corresponding to O_{48f} and O_{8a} with the area ratio of 40 %. In contrast, NMoZO and NSMoZO display symmetric, merged O1s peaks at 528.28 eV and 528.52 eV, respectively, with O_{8a} ratios of 30.87% and 37.6%. The lack of distinct peak splitting implies a homogenization of the oxygen coordination environments, attributed to increased cationic disorder arising from the substitution of Zr^{4+} with Mo^{6+} in NMoZO and co-doping with Sm^{3+} at the Nd site in NSMoZO. These substitutions likely induce antisite defects and lattice distortions, disrupting the regularity of the oxygen sublattice.

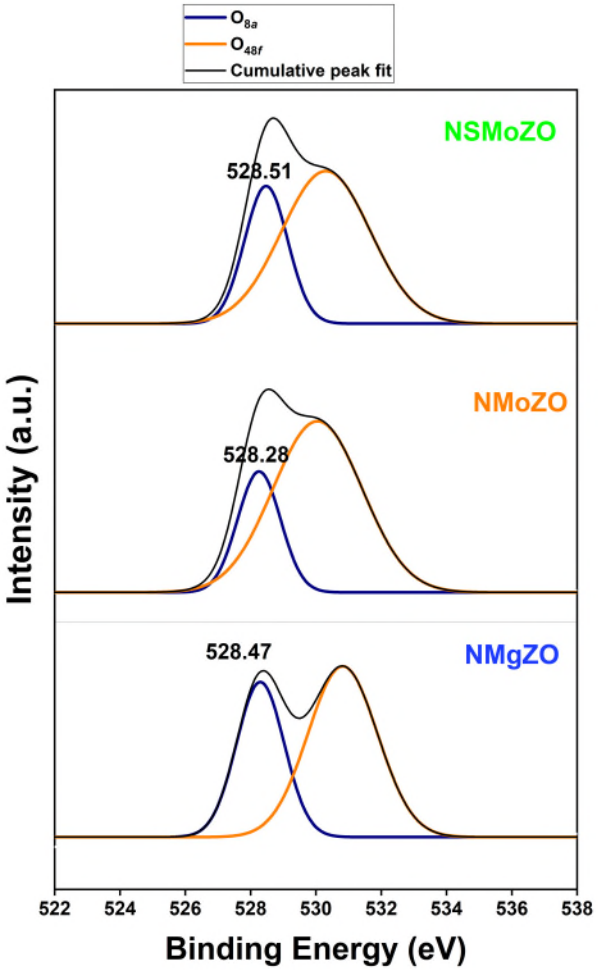


Figure 7: Deconvoluted O 1s spectra of doped samples.

The upward shift in binding energy observed in NSMoZO suggests a reduced electron density at oxygen sites, consistent with enhanced lattice polarization and a more covalent Mo–O bonding character. Collectively, NMgZO exhibits greater local structural order and electron density at oxygen sites, enabling efficient oxygen vacancy migration. In contrast, NMoZO and NSMoZO show merged oxygen environments due to cation disorder, which, while reducing site distinction, may still promote ionic conductivity by enhancing vacancy mobility through a more interconnected and disordered lattice.

3.6. Conductivity analysis

To confirm the performance of the developed electrolyte, the ionic conductivity was tested with respect to temperature. **Table 4** and **Figure 8**, shows the variations in ionic conductivities of the doped and co-doped zirconate samples in the intermediate temperature range of 500-750 °C. Ionic conductivity in these ceramics increases with temperature, indicating that oxide-ion transport is a thermally activated process. The doped and co-doped pyrochlore ceramics—NMgZO, NMoZO, and NSMoZO—exhibit enhanced ionic conductivity compared to undoped NZO (0.012 S/cm at 700 °C) [9]. Among them, NSMoZO shows slightly higher conductivity (0.0154 S/cm at 750 °C), followed by NMoZO (0.0152 S/cm at 750 °C) and NMgZO (0.0135 S/cm at 700 °C). NMoZO also maintains superior conductivity at lower temperatures, supported by the lowest activation energy (0.895 eV), indicating efficient oxygen ion transport, and the activation energy of the samples were close to the undoped NZO value of 0.8eV [15]. The observations made in the DFT calculations are similar to the experimental results obtained with ionic conductivity deviation very marginal similar to DFE deviation. NSMoZO with the lowest DFE (–5.742 eV), showed the highest ionic conductivity (0.0154 S/cm at 750 °C), while NMgZO having the highest DFE (–5.620 eV), exhibited the lowest (0.0107 S/cm) ionic conductivity. NMoZO, with an intermediate DFE (–5.739 eV), showed a comparable conductivity (0.0152 S/cm), at the same temperature. Although the DFE values differ only slightly, the experimental results show a clear trend, reinforcing the correlation between lower DFE and enhanced ionic transport.B-site doped samples show effective increase in the ionic conductivity; co-doped samples have trace improvement in conductivity. This observation reaffirms that ionic conductivity of the pyrochlore material can be altered significantly with the B-site doping, however A-site doping further promotes the oxygen migration.

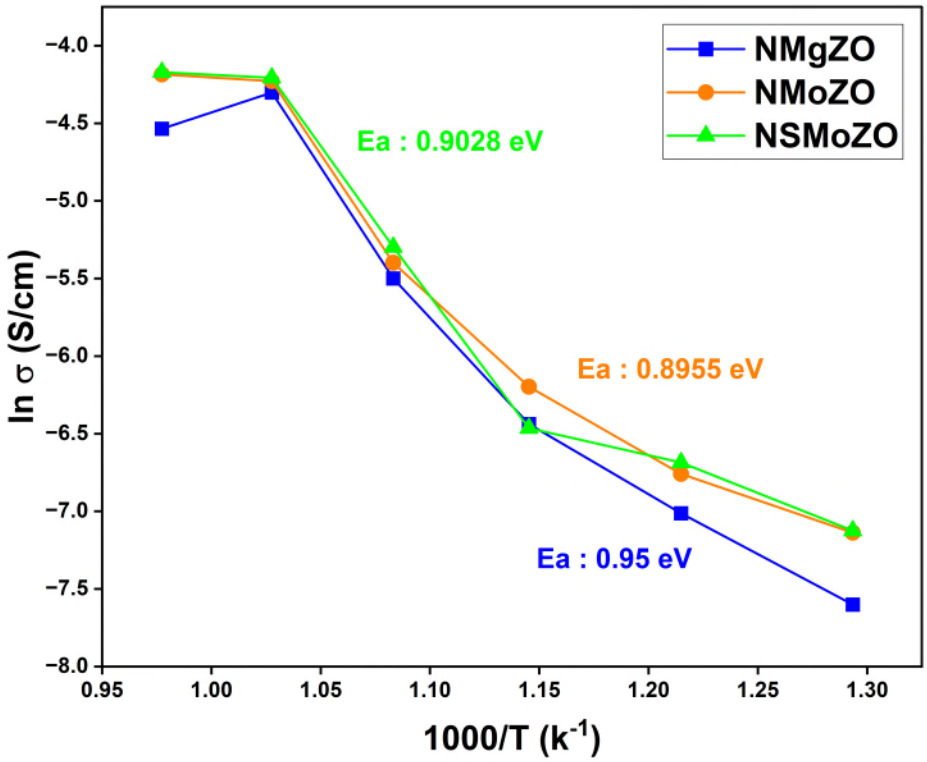


Figure 8: Arrhenius plots of the doped samples

In solid electrolytes, the overall conductivity is governed by the migration of oxygen ions via mobile oxygen vacancies [53]. Oxygen hopping occurs between adjacent anion sites, whose occupancy can be classified as O–V, V–O, O–O or V–V (where O denotes an oxide ion and V a vacancy), and these site-pair configurations dictate the ion-migration mechanism. Incorporation of Mg^{2+} into the Zr^{4+} sublattice of the pyrochlore structure results in the creation of oxygen vacancies to maintain charge neutrality, as Mg^{2+} carries a lower positive charge than Zr^{4+}. Each substitution introduces two negative effective charge, which is compensated by the formation of one doubly charged oxygen vacancy ($V_O^{\cdot\cdot}$), shown in **Equation 11**. This defect mechanism also causes lattice expansion, thereby increasing the overall unit cell volume of the

pyrochlore. In contrast, when Mo^{6+} substitutes for Zr^{4+}, it introduces a +2-charge excess. The lattice compensates this imbalance by creating one $V_O^{\cdot\cdot}$ to restore charge neutrality. Additionally, two lattice oxygen ions $O_O^{\times}$ are added to account for the oxygen from MoO_3, shown in **Equation 12**.

$$MgO \rightarrow Mg''_{Zr} + V_O^{\cdot\cdot} + O_O^{\times} \quad (11)$$

$$MoO_3 \rightarrow Mo^{\cdot\cdot}_{Zr} + V_O^{\cdot\cdot} + 2O_O^{\times} \quad (12)$$

In Mg-doped samples, higher levels of Mg substitution at the Zr site may result in partial occupancy of the A site by Mg, which can limit the formation of oxygen vacancies. The substitution of Zr^{4+} (ionic radius ~0.72 Å) by the smaller Mo^{6+} cation (ionic radius ~0.59 Å) leads to partial occupation of the 8b site by O^{2-} ions, thereby generating oxygen vacancies at the 48f site. These vacancies are essential for facilitating the oxide-ion hopping mechanism within the pyrochlore lattice [54]

Table 4: Ionic conductivity and activation energy data of the doped samples

Temperature (° C)	**Ionic conductivity (S/cm)**		
	NMgZO	**NMoZO**	**NSMoZO**
500	0.0005	0.0007	0.0008
550	0.0009	0.0011	0.0012
600	0.0016	0.0020	0.0015
650	0.0040	0.0045	0.0050

700	0.0135	0.0145	0.0148
750	0.0107	0.0152	0.0154
Activation energy Ea (eV)	0.95	0.895	0.9028

Defect formation energy (DFE) calculations reveal that Mo (–5.6827 eV) and Sm (–5.7460 eV) facilitate oxygen vacancy generation, essential for ionic conduction. Although NMoZO benefits from low DFE and activation energy, its lower g-factor suggests partial immobilization or non-paramagnetic vacancies. EPR spectroscopy confirms the vacancy generation with NSMoZO exhibiting the highest g-factor (2.2092), implying the greatest vacancy concentration. Moreover, the lowest dislocation density and lattice strain along with a higher relative density of the particle with a lesser porous structure, suggest the favourable structural parameters for ion migration. The synergy between Sm and Mo co-doping enhances both vacancy formation and mobility, leading to optimal conductivity in NSMoZO. Mo substitution on the B-site elevates the oxygen ion mobility ($V_O^{\cdot\cdot}$) through aliovalent charge compensation, and Sm substitution on the A-site preserves the long-range pyrochlore lattice integrity by suppressing defect clustering and maintaining the pyrochlore structural framework for sustained vacancy mobility. The results obtained in this study demonstrate that the co-doped system achieves a balanced combination of structural disorder, low activation energy, and high vacancy concentration—key to improved ionic transport. Simple substation of A-site or B-site alone need not achieve the structural stability along with oxygen migration, rather the synergistic effect leads to improved performance. These synergistic effect are due to combination of structural, morphological and thermodynamic dependent, a simple

experimental-based study doesn't lead to the optimized combination; a theoretical study could aid the dopant selection and composition optimization more easily.

This work combines first-principles defect formation energy calculations with characterization tools like, XRD, SEM, EPR, and XPS, along with two-probe ionic conductivity measurement that constitutes a reliable methodology for the rational design of high-performance oxide-ion conductors. The conductivity values achieved, particularly for NSMoZO and NMoZO, represent a significant advancement over undoped NZO and establish co-doping as credible means to improve the electrolyte performance for IT-SOFC operation in the 600–750°C range. Future work on advanced doping strategies or microstructural tuning to fully exploit the potential of these materials for solid-state ionic applications would improve the prospect of pyrochlore-based electrolyte SOFC system.

4. Conclusions

Pyrochlore materials, especially rare-earth zirconates represents a highly promising class of materials for SOFC electrolytes in particular for the development of efficient and durable IT-SOFCs. This study successfully demonstrated that rational co-doping $Nd_2Zr_2O_7$ pyrochlore on both A and B sites is a powerful and computationally predictable strategy for optimizing oxygen-ion conductivity in pyrochlore materials. First-principal DFT calculations precisely identified 10 % B-site doping of Mo and Mg on NZO shows the lowest DFE and co-doping of $Nd_{1.9375}Sm_{0.06251}Zr_{1.7}Mo_{0.30}O_7$ as an optimized composition, exhibiting a favorable defect formation energy of -5.742 eV, indicative of facile oxygen vacancy generation. This theoretical prediction was strongly corroborated by experimental results. Among the synthesized samples $Nd_2Zr_{1.7}Mg_{0.3}O_7$ (NMgZO), $Nd_2Zr_{1.7}Mo_{0.3}O_7$ (NMoZO) and $Nd_{1.9375}Sm_{0.06251}Zr_{1.7}Mo_{0.30}O_7$ (NSMoZO), NSMoZO consistently achieved the highest ionic

conductivity of 0.0154 S/cm at 750 °C. NMoZO also showed excellent performance with 0.0152 S/cm at 750 °C and the lowest activation energy (0.895 eV), indicating efficient oxygen ion transport. The enhanced conductivity is directly attributed to the creation and efficient mobility of oxygen vacancies ($V_O^{\cdot\cdot}$), facilitated by aliovalent doping and structural features that favors ion migration. EPR spectroscopy confirmed that NSMoZO possessed the highest vacancy concentration, XRD-derived structural parameters together with SEM analysis establish that consistent structure-property accounts to the favourable ionic conductivity of NSMoZO. The synergistic effect of Sm and Mo co-doping was crucial, Mo modifies the diosrered structure, and Sm affects the structural stability and thus improves oxygen ion mobility. The DFT-based defect formation energy framework is validated as a reliable and computationally efficient descriptor for dopant pre-screening in rare-earth zirconate pyrochlores, establishing a transferable computation-first design paradigm for accelerating oxide-ion conducting electrolyte discovery across the broader IT-SOFC materials landscape.

Author contributions

AA: Methodology, Validation, Formal analysis, Visualization, Investigation, Data curation, Writing- original draft, review & editing, and Visualization. **APA:** Conceptualization, Methodology, Formal analysis, Resources, Visualization, Supervision, Project administration, Funding acquisition and Writing- original draft, Writing review & editing.

Conflicts of interest

None of the authors have a conflict of interest to disclose

Data availability

A supporting document is included, which provides the data used in the article.

Acknowledgements

The Project is financially supported by ANRF (formerly SERB) through the grant SRG/2021/000654. The authors thank Indian Science Technology and Engineering facilities Map (I-STEM), a Program supported by Office of the Principal Scientific Adviser to the Govt. of India, for enabling access to the PXRD (make: XPERT-PRO), FESEM (make: JEOL JSM-IT800), EPR (make: EOL RESONANCE Inc. JES-FA100 spectrometer) at National Institute of Technology, Warangal to carry out the characterization work. Also thanks Central Research Facility of Indian Institute of Technology, Delhi for XPS data.

References

1. Zou P, Iuga D, Ling S, et al (2024) A fast ceramic mixed OH−/H+ ionic conductor for low temperature fuel cells. Nat Commun 15:. https://doi.org/10.1038/s41467-024-45060-1
2. Singhal SC (2007) Solid oxide fuel cells. Electrochemical Society Interface 16:41–44. https://doi.org/10.1533/9781845690815.2.140
3. Singh M, Zappa D, Comini E (2021) Solid oxide fuel cell: Decade of progress, future perspectives and challenges. Int. J. Hydrogen Energy 46:27643–27674
4. Anantharaman AP, Prasad H (2020) Potential of pyrochlore structure materials in solid oxide fuel cell applications. Ceram Int 47:4367–4388. https://doi.org/10.1016/j.ceramint.2020.10.012

5. Fergus JW (2006) Electrolytes for solid oxide fuel cells. J Power Sources 162:30–40. https://doi.org/10.1016/j.jpowsour.2006.06.062

6. Subramanian MA, Aravamudan G, Subba Rao G V. (1983) Oxide pyrochlores — A review. Progress in Solid State Chemistry 15:55–143. https://doi.org/10.1016/0079-6786(83)90001-8

7. Kong L, Karatchevtseva I, Gregg DJ, et al (2013) A novel chemical route to prepare La2Zr2O7 pyrochlore. Journal of the American Ceramic Society 96:935–941. https://doi.org/10.1111/jace.12060

8. Koteswara Rao K, Banu T, Vithal M, et al Preparation and characterization of bulk and nano particles of La 2 Zr 2 O 7 and Nd 2 Zr 2 O 7 by sol-gel method

9. Raj A A, Anantharaman AP (2024) Exploring the defect formation and ionic migration in A2Zr2O7 (A = La, Ce, Nd, and Gd) Pyrochlore solid-state electrolytes. Ceram Int 50:48116–48126. https://doi.org/10.1016/j.ceramint.2024.09.162

10. Vendrell X, West AR (2018) Electrical Properties of Yttria-Stabilized Zirconia, YSZ Single Crystal: Local AC and Long Range DC Conduction. J Electrochem Soc 165:F966–F975. https://doi.org/10.1149/2.0881811jes

11. Nyman BJ, Björketun ME, Wahnström G (2011) Substitutional doping and oxygen vacancies in La2Zr 2O7 pyrochlore oxide. Solid State Ion 189:19–28. https://doi.org/10.1016/j.ssi.2011.01.013

12. Sadykov VA, Sadovskaya EM, Filonova EA, et al (2020) Oxide ionic transport features in Gd-doped La nickelates. Solid State Ion 357:. https://doi.org/10.1016/j.ssi.2020.115462

13. Liu Z, Ouyang J, Sun K, et al (2012) Influence of magnesia doping on structure and electrical conductivity of pyrochlore type GdSmZr2O7. Advances in Applied Ceramics 11:214–219. https://doi.org/10.1179/1743676111Y.0000000077

14. Moreno KJ, Mendoza-Suárez G, Fuentes AF, et al (2005) Cooperative oxygen ion dynamics in Gd2Ti2-yZryO7. Phys Rev B Condens Matter Mater Phys 71:. https://doi.org/10.1103/PhysRevB.71.132301

15. Mandal BP, Deshpande SK, Tyagi AK (2008) Ionic conductivity enhancement in Gd2Zr2O7 pyrochlore by Nd doping. J Mater Res 23:911–916. https://doi.org/10.1557/jmr.2008.0112

16. Xia XL, Liu ZG, Ouyang JH, et al (2011) Effect of Ce substitution for Zr on electrical property of fluorite-type Gd2Zr2O7. Solid State Sci 13:1328–1333. https://doi.org/10.1016/j.solidstatesciences.2011.04.001

17. Radhakrishnan AN, Rao PP, Mahesh SK, et al (2012) Role of bond strength on the lattice thermal expansion and oxide ion conductivity in quaternary pyrochlore solid solutions. Inorg Chem 51:2409–2419. https://doi.org/10.1021/ic202383f

18. Zhu L, Wang Y, Chen J, et al (2022) Enhancing ionic conductivity in solid electrolyte by relocating diffusion ions to under-coordination sites

19. Kuwabara A, Tanaka I (2004) First principles calculation of defect formation energies in Sr- and Mg-doped LaGaO3. Journal of Physical Chemistry B 108:9168–9172. https://doi.org/10.1021/jp049808m

20. Zhao J, Liu Y, Fan Y, et al (2021) Native point defects and oxygen migration of rare earth zirconate and stannate pyrochlores. J Mater Sci Technol 73:23–30. https://doi.org/10.1016/j.jmst.2020.09.033

21. Kang J, Feng W, Guo D, et al (2022) Performance optimization of Ca and Y co-doped CeO2-based electrolyte for intermediate-temperature solid oxide fuel cells. J Alloys Compd 913:. https://doi.org/10.1016/j.jallcom.2022.165317

22. Kanghee J, Ha J, Ryu J, et al (2021) DC 4-Point Measurement for Total Electrical Conductivity of SOFC Cathode Material. Appl Sci 2021:4963. https://doi.org/10.3390/app

23. Satheeshkumar E, Prabunathan P, Anbarasi P, et al (2020) Temperature dependent electrical properties of YSZ synthesized through microwave combustion. Appl Phys A Mater Sci Process 126:1–11. https://doi.org/10.1007/s00339-020-03893-9

24. Hieu HK, Lam LT (2025) New insights into the dopant size-ionic transport relationship for Ln2O3-doped Ceria (Ln = Yb, Er, Ho, Y, Dy, Gd, Eu, Sm, Nd, and La) electrolytes through statistical moment calculations. Mater Sci Semicond Process 190:. https://doi.org/10.1016/j.mssp.2025.109317

25. Anokhina IA, Animitsa IE, Voronin VI, et al (2021) The structure and electrical properties of lithium doped pyrochlore Gd2Zr2O7. Ceram Int 47:1949–1961. https://doi.org/10.1016/j.ceramint.2020.09.025

26. Sayed FN, Mandal BP, Jain D, et al (2012) Improved ionic conductivity in NdGdZr 2O 7: Influence of Sc 3+ substitution. J Eur Ceram Soc 32:3221–3228. https://doi.org/10.1016/j.jeurceramsoc.2012.03.038

27. Díaz-guillén JA, Fuentes AF, Díaz-guillén MR, et al (2009) The effect of homovalent A-site substitutions on the ionic conductivity of pyrochlore-type Gd2Zr2O7. J Power Sources 186:349–352. https://doi.org/10.1016/j.jpowsour.2008.09.106

28. Lee HC, Kim D, Lee JA, et al (2022) Oxygen migration energy in La and Y Co-doped CeO2: Effect of lattice constant and grain boundary segregation. Journal of Science: Advanced Materials and Devices 7:. https://doi.org/10.1016/j.jsamd.2022.100450

29. Belov DA, Shlyakhtina A V., Stefanovich SY, et al (2009) Acceptor doping of Ln2Ti2O7 (Ln = Dy, Ho, Yb) pyrochlores with divalent cations (Mg, Ca, Sr, Zn). Mater Res Bull 44:1613–1620. https://doi.org/10.1016/j.materresbull.2009.04.013

30. Nakamura K, Mori M, Itoh T, Ohnuma T (2016) Theoretical and experimental investigation of defect formation / migration in Gd2Ti2O7: General rule of oxide-ion migration in A2B2O7 pyrochlore. AIP Adv 6:. https://doi.org/10.1063/1.4967211

31. Vendrell X, Santos-Veiga EL, Beltrán-Mir H, et al (2023) Induced p-type semiconductivity in Mg-doped Nd2Zr2O7 pyrochlore system. J Eur Ceram Soc 43:6967–6973. https://doi.org/10.1016/j.jeurceramsoc.2023.07.061

32. Lyskov N V., Kolbanev I V., Borunova AB, et al (2025) Study of Mg doping on the zirconium and lanthanide sites of Ln2Zr2O7 (Ln = Sm, Gd) pyrochlores. Ceram Int 51:32808–32820. https://doi.org/10.1016/j.ceramint.2025.05.015

33. Patwe SJ, Ambekar BR, Tyagi AK (2005) Synthesis, characterization and lattice thermal expansion of some compounds in the system Gd2CexZr2-xO 7. J Alloys Compd 389:243–246. https://doi.org/10.1016/j.jallcom.2004.06.094

34. Feighery AJ, Irvine JTS, Zheng C (1997) High Oxide Ion Conductivity in Non-Stoichiometric Pyrochlores and Fluorites in the Ternary System ZrO2-Gd203-TiO

35. Kumar SC, Madhavan B, S P, et al (2025) Enhanced oxygen ion conductivity in La2Zr2-xTixO7 based pyrochlore electrolyte for intermediate temperature solid oxide fuel cell fabrication. Mater Chem Phys 344:. https://doi.org/10.1016/j.matchemphys.2025.131188

36. Moon PK, Tuller HL (1988) Ionic conduction in the Gd2Ti2O7−Gd2Zr2O7 system. Solid State Ion 28–30:470–474. https://doi.org/10.1016/S0167-2738(88)80085-7

37. Liu ZG, Gao S, Ouyang JH, Xia XL (2010) Influence of MoO3 doping on structure and electrical conductivity of defect fluorite-type Gd2Zr2O7. J Alloys Compd 506:868–871. https://doi.org/10.1016/j.jallcom.2010.07.101

38. Anokhina IA, Animitsa IE, Voronin VI, et al (2021) The structure and electrical properties of lithium doped pyrochlore Gd2Zr2O7. Ceram Int 47:1949–1961. https://doi.org/10.1016/j.ceramint.2020.09.025

39. Anokhina IA, Animitsa IE, Buzina AF, et al (2020) Synthesis, structure and electrical properties of Li+-doped pyrochlore Gd2Zr2O7. Chimica Techno Acta 7:51–60. https://doi.org/10.15826/chimtech.2020.7.2.02

40. Liu ZG, Gao S, Ouyang JH, Xia XL (2010) Influence of MoO3 doping on structure and electrical conductivity of defect fluorite-type Gd2Zr2O7. J Alloys Compd 506:868–871. https://doi.org/10.1016/j.jallcom.2010.07.101

41. Qu Z, Wan C, Pan W (2007) Thermal expansion and defect chemistry of MgO-doped Sm2Zr 2O7. Chemistry of Materials 19:4913–4918. https://doi.org/10.1021/cm071615z

42. Kramer S, Spears M, Tuller HL (1994) Conduction in titanate pyrochlores : role of dopants. Solid State Ion 72:59–66

43. Kramer S, Spears M, Tuller HL (1994) Conduction in titanate pyrochlores: role of dopants. Solid State Ion 72:59–66. https://doi.org/10.1016/0167-2738(94)90125-2

44. Xiong XZ, Liu ZG, Ouyang JH, et al (2011) Preparation, structure and electrical conductivity of the pyrochlore-type phase Sm2Zr2O7 codoped with bivalent magnesium and trivalent dysprosium cations. J Alloys Compd 509:8392–8397. https://doi.org/10.1016/j.jallcom.2011.05.088

45. Wen LC, Li ZP, Chen HS, Tseng SC (2023) Preparation and electrical properties of pyrochlore R2(ZrTi)O7 for solid oxide fuel cell electrolyte. J Energy Storage 64:. https://doi.org/10.1016/j.est.2023.107058

46. Kong L, Karatchevtseva I, Gregg DJ, et al (2013) Gd2Zr2O7 and Nd2Zr2O7 pyrochlore prepared by aqueous chemical synthesis. J Eur Ceram Soc 33:3273–3285. https://doi.org/10.1016/j.jeurceramsoc.2013.05.011

47. Alzamani M, Jafarzadeh K, Fattah-alhosseini A (2021) Development of lanthanum doped Ni10Cu11Fe6Al as a new inert anode in molten salt calcium chloride for titanium oxide electrolysis. J Alloys Compd 876:. https://doi.org/10.1016/j.jallcom.2021.159997

48. Hagiwara T, Yamamura H, Nishino H (2011) Relationship between oxide-ion conductivity and ordering of oxygen vacancy in the Ln2Zr2O7 (Ln La, Nd, Eu) system having a pyrochlore composition. In: IOP Conference Series: Materials Science and Engineering

49. Guo L, Guo H, Gong S (2013) The ordering degree and thermal conductivity in the pyrochlore-type composition systems with a constant cation radius ratio. Mater Lett 106:119–121. https://doi.org/10.1016/j.matlet.2013.05.020

50. Qiao H, He C, Wang Z, et al (2018) Improved thermal stability of ferro/piezo-electric properties of Mn-doped Pb(In1/2Nb1/2)O3-PbTiO3 ceramics. J Eur Ceram Soc 38:3162–3169. https://doi.org/10.1016/j.jeurceramsoc.2018.02.040

51. Chen H, Wang Y, Wang G, et al (2024) Insights in the phase stability and performance enhancement mechanism of La2(Zr1-xCex)2O7 with reduced thermal conductivity. J Alloys Compd 991:. https://doi.org/10.1016/j.jallcom.2024.174575

52. Chen J, Lian J, Wang LM, et al (2002) X-ray Photoelectron Spectroscopy Study of Disordering in Gd 2ʿTi 1 2 x Zr xˆ2 O 7 Pyrochlores. Phys Rev Lett 88:1–4. https://doi.org/10.1103/PhysRevLett.88.105901

53. Zhang C, Li CJ, Zhang G, et al (2007) Ionic conductivity and its temperature dependence of atmospheric plasma-sprayed yttria stabilized zirconia electrolyte. Materials Science and Engineering: B 137:24–30. https://doi.org/10.1016/j.mseb.2006.10.005

54. Yang F, Wang Y, Zhao X, Xiao P (2015) Enhanced ionic conductivity in pyrochlore and fluorite mixed phase yttrium-doped lanthanum zirconate. J Power Sources 273:290–297. https://doi.org/10.1016/j.jpowsour.2014.09.067

Supplementary Files

This is a list of supplementary files associated with this preprint. Click to download.

- Supportingdocument02.02.2026.docx
- GraphicalAbstract.tif